MIT Open Access Articles

A low-dissipation, pumpless, gravity-induced flow battery

A Low-Dissipation, Pumpless, Gravity-Induced Flow Battery†

Xinwei Chen[a, #], Brandon J. Hopkins[b, #], Ahmed Helal[b], Frank Y. Fan[a], Kyle C. Smith[a], Zheng Li[a], Alexander H. Slocum[b], Gareth H. McKinley[b], W. Craig Carter[a], Yet-Ming Chiang[a,*]

† Electronic Supplementary Information (ESI) available.

[(a)] Department of Materials Science and Engineering and [(b)] Department of Mechanical Engineering, Massachusetts Institute of Technology, Cambridge, Massachusetts 02139, United States

[#]Equal contribution

* Corresponding author

- Telephone number: (617) 253-6471

- E-mail: ychiang@mit.edu

Abstract

Redox flow batteries have the potential to provide low-cost energy storage to enable renewable energy technologies such as wind and solar to overcome their inherent intermittency and to improve the efficiency of electric grids. Conventional flow batteries are complex electromechanical systems designed to simultaneously control flow of redox active fluids and perform electrochemical functions. With the advent of redox active fluids with high capacity density, i.e., Faradaic capacity significantly exceeding the 1-2 M concentration equivalents typical of aqueous redox flow batteries, new flow battery designs become of interest. Here, we design and demonstrate a proof-of-concept prototype for a "gravity-induced flow cell" (GIFcell), representing one of a family of approaches to simpler, more robust, passively driven, lower-cost flow battery architectures. Such designs are particularly appropriate for semi-solid electrodes comprising suspensions of networked conductors and/or electroactive particles, due to their low energy dissipation during flow. Accordingly, we demonstrate the GIFcell using nonaqueous lithium polysulfide solutions containing a nanoscale carbon network in a half-flow-cell configuration, and achieved round trip energy efficiency as high as 91%.

Broader context

The advent of new flow battery chemistries having higher energy density than typical aqueous flow electrodes offers an opportunity for re-thinking flow battery design. Here, a novel flow battery that is conceptually analogous to an hourglass of variable tilt angle is designed and tested. Using gravity to drive flow, and a combination of cell geometry, surface engineering, and gas-flow control to control flow rate, the GIFcell is demonstrated using an electronically-conductive lithium polysulfide-nanocarbon catholyte against a stationary lithium metal electrode. The GIFcell represents a first example of what we believe will be a new class of passively-driven flow battery concepts that provide greater simplicity and reliability than conventional flow battery designs.

1.   Introduction

Low-cost, scalable energy storage is crucial to the integration of sustainable but intermittent energy generation technologies such as wind and solar into the electric power infrastructure. Redox flow batteries are amongst the technologies that may meet these needs, due to their ability to decouple stored energy from power, inherent scalability, and potential for low cost[1-4]. Existing flow batteries designed to operate with low energy density aqueous solution flow electrodes of 1-2 M redox active concentration (also termed catholyte and anolyte),[5,6] are relatively complex electrochemical-mechanical systems in which a high part count has historically compromised reliability and cost. Despite about thirty years of development, the basic architecture of the flow battery has not changed. With the advent of high energy density flow electrodes, such as the semi-solid lithium ion suspensions pioneered by Duduta et al.[7] and the electronically-conductive lithium polysulfide solution/precipitation flow electrodes developed by Fan et al.[8], opportunities to re-invent the conventional flow battery have arisen. We are motivated by these new flow electrode capabilities to explore potentially more efficient, passively driven, compact, simpler and lower-cost flow battery architectures.

Here, we develop and demonstrate one such concept, a pumpless design that utilizes gravity to induce flow (Fig. 1) referred to herein as a gravity-induced flow cell (GIFcell). Conceptually analogous to an hourglass of variable tilt angle, gravitational force causes flow of energy-dense electrodes through a centrally positioned electrochemical stack. Reversal of flow is carried out by physically inverting the GIFcell. Each half-cycle of the battery, whether charge or discharge, may be conducted with multiple passes, or in theory a single pass (i.e., "stoichiometric" flow)[9]. In this paper, we identify the most important design parameters for such a flow battery through modeling

and experiment, and demonstrate a prototype specifically designed for energy-dense, rheologically complex non-Newtonian flow electrodes.

For stationary flow battery applications, a more energy-dense chemistry not only reduces system size, but can lower system cost and improve efficiency and reliability. As we show, the mechanical loss in operating the GIFcell is a very small fraction of the stored electrochemical energy of the battery. This is not surprising since a fundamental advantage of electrochemical storage is its much higher energy density compared to mechanical approaches (e.g., pumped hydroelectric storage). Although the GIFcell can be scalable to large size without sacrificing this fundamental mechanical efficiency, the availability of compact modular flow cells permits new design flexibility, including highly networked architectures not possible with conventional flow batteries. Systems of large total energy could be composed of parallel/series networks of individual cells, each of which has variable power output (through tilt angle) and can be easily switched, providing redundancy and improving the reliability of the network.

2. Design of Lithium Polysulfide Flow Electrodes

Although the GIFcell concept can in principle be applied broadly to the expanding number of flowable, energy-storing solutions and suspensions,[7,8,10] we focus here on high energy density flow electrodes which will tend to have higher viscosities compared to typical aqueous flow electrolytes of low molar concentration, such as vanadium redox solutions (20-70 cP)[8]. Furthermore, non-Newtonian rheology is likely to be the rule rather than the exception at high concentrations of redox active species. To illustrate the special considerations that must be taken into account when designing for complex rheology, we use lithium-sulfur as the experimental chemistry. As the positive electrode, we use the electronically-conductive lithium polysulfide

suspensions developed by Fan et al.,[8] wherein percolating nanocarbon suspensions provide an extended, in-situ, current collector network enabling charge-transfer throughout the volume of the flow electrode. For the negative electrode, we use a stationary lithium metal foil as was used in ref. 8. As shown later, the use of the stationary lithium metal electrode leads to impedance growth and cycling fade issues that are well-known to those in the field of Li-S batteries. However, this "half-flow-cell" design in which only the cathode flows allows the operation of the GIFcell to be evaluated in a simpler design than a "full-flow cell" (our ultimate goal) in which both electrodes flow.

The sulfur flow electrode does not contain solid elemental sulfur but rather contains Li_2S_8, which is completely soluble in the solvent phase. Fig. 2a shows the voltage-capacity behavior of the Li-Li_2S_8 couple when operated over a complete galvanostatic charge-discharge cycle in a stationary cell. A very high specific capacity of ~1000 mAh/g-S is obtained since the sulfur positive electrode is cycled between the composition limits Li_2S_8 (dissolved) and Li_2S (solid); the incorporation of the nanoscale conductor network permits charge-transfer throughout the volume of the electrode and allow sulfur utilization over both the solution-phase and precipitation (of Li_2S) regimes. However, in the flow cell experiments, we limited the range of the cathode reaction to the fully-soluble regime between Li_2S_8 and Li_2S_6 (Fig. 2a), to minimize rheological changes that accompany the precipitation of solid Li_2S. Thus the overall cell reaction used is $2Li + 3Li_2S_8 \rightarrow 4 Li_2S_6$.

At low concentrations (0.5-2.0 vol%) of the percolating carbon network, electronic conductivities of 2.5-18 mS/cm are achievable in the flow electrode (plotted in Fig. S8 of ref. 8), which exceed typical ionic conductivities for the nonaqeuous electrolyte. These flow electrodes have Hershel-Bulkley rheology wherein the fluid has a finite yield stress as well as shear-thinning

behavior. The rheology of the present flow electrodes at 0.5% and 1.5% carbon are compared in Fig. S1, ESI, with that of ketchup, another well-known yield stress fluid that presents similar challenges in obtaining stable, controlled flow during use.

The basic formulation of the semi-solid flow cathode consists of a solution phase containing Li_2S_8 dissolved in a glyme solvent, with 0.5 M LiTFSI and 1 wt% of $LiNO_3$ being added as the supporting salt and solid electrolyte interphase (SEI) formation additive, respectively, and into which is dispersed <1% by volume of a nanoscale carbon. Rheology and electrochemical performance are strongly dependent on composition. Solvent choice is a trade-off between volatility, viscosity and electrochemical function; within the glyme family, diglyme showed the highest capacity and lowest polarization (Fig. 3a), but has too high a vapor pressure for consistent experimentation (Table 1). Exchange current density measurements of Li_2S_6 solutions show an order of magnitude decrease in interfacial reaction rate on glassy carbon between the endmembers diglyme and tetraglyme (results to be reported elsewhere). On the other hand, all three glymes tested have similar viscosities at a constant carbon black loading (Fig. 3b). Therefore, the triglyme electrolyte was chosen as the most suitable compromise between low volatility and facile electrochemical kinetics.

The yield stress and viscosity of the semi-solid catholyte are most strongly dependent on the carbon black content, as shown in Fig. 3c for triglyme solvent. The yield stress increases by a factor of 100 between 0.25% and 1% carbon by volume, which strongly limits gravitational flow. However, higher nano-carbon content also increases electronic conductivity, which in turn can improve electrochemical kinetics. Fig. 3d shows the yield stress vs electronic conductivity of the flow electrode using triglyme solvent. Separate experimentation showed that adequate electrochemical kinetics could be achieved over a range of carbon contents, and that the limiting

factor is yield stress-controlled gravitational flow (i.e., by analogy to the flow of ketchup, too high a yield stress prevents flow under the force of gravity alone; in the ketchup bottle instance the yield stress is overcome by additional acceleration). Assuming a stress-free interface with no slip of the fluid at the wall, the wall shear-stress in the flow electrode is given by:

$$\tau_w = \rho g \sin\theta \frac{H}{2} \qquad (1)$$

where τ_w is the shear stress at the wall, ρ is the density of the suspension, g is the acceleration due to gravity, H is the thickness of the fluid film, and θ is the angle of the GIFcell from the horizontal plane (to which gravity is normal). The notations for the GIFcell are shown in Fig. 2c. The critical angle for the onset of flow, θ_o, occurs when the shear stress at the wall, τ_w, reaches the yield stress of the suspension, $\tau_w = \tau_y$, and is given by:

$$\theta_O = \sin^{-1}(\frac{2\tau_y}{\rho g H}) \qquad (2)$$

Fig. 3d shows color contours giving the critical flow angle corresponding to the yield stresses shown, assuming $H = 1.6$ mm. In order to allow for a wide range of flow angles ($\theta_O \leq 15°$), the carbon loading was thus chosen to be 0.5 vol%. This 0.5 vol% carbon flow electrode, containing 2.5 M S/L of Li_2S_8 in triglyme with 0.5 M LiTFSI and 1 wt% $LiNO_3$, has nearly identical electronic and ionic conductivity of ~2.5 mS/cm, and is an ideal mixed-conductor. The suspension was measured to have the following Herschel-Bulkley parameters (curve fit to $R^2 = 0.99$): Yield stress is $\tau_y = 1.33$ Pa, consistency is $K = 4.487$ Pa.s^n and power-law index is $n = 0.59$. For simpler flow modeling, a piecewise Bingham model can also be fit to the rheometric data in Fig. 3c to $R^2 = 0.99$, as explained in the ESI and Fig. S2.

3.   Design of a Prototype GIFcell

3.1   Avoiding Flow Instability

The prototype is based on a channel of constant rectangular cross-section, see Fig. 2b, firstly because a channel without constrictions minimizes yield stress inhibition of flow, and secondly because a rectangular cross section permits use of simple planar current collectors. The channel volumes on either side of the electroactive zone represent the flow battery "tanks," and were designed to have about four times the volume of the current collecting "stack" in between. In this design, it is desirable for the electrode to flow with a uniform flow front, in order to promote uniform charge and discharge of the flow electrode and avoid entrainment of bubbles. However, experiments showed that such cross-sections can undergo a Saffman-Taylor flow instability[11–13], also known as "viscous fingering" (Fig. 4). A suitable channel geometry was identified by performing flow tests using the selected suspension in a Hele-Shaw test cell as shown in Fig. 4. (Movie S1 in ESI shows the flow stability tests for various channel dimensions.) The Saffman-Taylor instability was suppressed by narrowing the ratio of channel width to height, W/H; for $H = 1.6$ mm, a suitable cross-section dimension identified from electrochemical testing, the critical channel width was found to be $W \simeq 13$ mm. For subsequent experiments, the channel width was selected to be slightly smaller at $W = 10$ mm. Other techniques such as grading the height of the channel could also be used to suppress the flow instability[14]; but may complicate flow rate and electrokinetic control.

3.2   Characterizing Wall Slip

Despite designing the suspension for flow in the absence of wall slip, the introduction of high slip surfaces is beneficial as it allows the carbon black containing suspension to flow

unyielded as a plug even at lower tilt angles, permitting flow control and higher electrochemical efficiency over a wider range of operating conditions[9]. We explored the impact of wall slip on flow cell design using an analytical model and corroborating experiments.

Although a no-slip boundary condition is typically used in flow modeling for Newtonian fluids[15], yield stress fluids and suspensions have been shown to exhibit wall slip[16–18]. Surfaces of low energy and those with which the suspension has a high contact angle are likely to exhibit stronger slip at the wall[19]. For the glyme-based flow cathodes used here, PTFE (Teflon®) proved to be a useful high slip surface, as characterized in Fig. 5a and illustrated in Fig. S3 and Movie S2 (ESI). To examine the impact of wall slip on cell design, two model surfaces were compared; a stainless steel surface exhibiting no wall slip and the Teflon® surface.

Using a torsional rheometer with a parallel plate geometry, the slip velocity was determined using the multiple gap slip correction model proposed by Yoshimura & Prud'Homme [20] (ESI). The slip velocity V_s of our model suspension is shown in Fig. 5a as a function of the applied shear stress τ for the stainless steel and Teflon® surfaces. The stainless steel surface was found to exhibit no wall slip within the range of stress accessible through the measurement. For the Teflon® surface, above a critical stress τ_c, a finite slip velocity that increases linearly with applied stress was observed. The critical stress τ_c is associated with the work needed for adhesive failure at the wall surface and onset of slip. As seen from Movie S2, a droplet of the polysulfide catholyte was able to glide freely on a Teflon® surface but not on the acrylonitrile butadiene styrene (ABS) material from which the flow cell bodies were fabricated (by 3D printing). We measured the advancing and receding contact angles of a 0.5 vol% KB suspension on the Teflon® to be 71.4º and 70.9º respectively (Fig. S4, ESI).

Next, the slip parameters were quantified from experiment. Wall slip behavior was modeled using a critical slip model [21,22] given by:

$$\tau < \tau_c, V_s = 0 \tag{3}$$

$$\tau \geq \tau_c, V_s = \beta(\tau - \tau_c) \tag{4}$$

where τ_c is the critical stress for onset of slip and β is the slip coefficient. A fit of this model to the experimental data on the Teflon® surface is shown in Fig. 5a ($R^2 = 0.95$); the critical stress and slip coefficient were found to be $\tau_c = 0.78$ Pa and $\beta = 205$ μ m. $\mathrm{Pa}^{-1}.\mathrm{s}^{-1}$ respectively.

3.3   Modeling Flow vs Tilt Angle for No-Slip and High Slip Surfaces

With these parameters in hand, the impact of slip on the flow velocity vs. tilt angle behavior of the rectangular flow channel was modeled. Flow of the suspension in a channel of gap H (the distance between the current collectors), length L, and width W was modeled (Fig. 5b). The geometry of the cell has $H \ll L$, $W \ll L$, and flow is assumed to be two-dimensional with no fingering instabilities or capillary effects such as contact line-pinning. Two slip boundary conditions were modeled, either no-slip or the critical slip model described above. The equation of motion for the yield stress fluid is solved analytically [22] and the flow rate, Q (cm³/s), was obtained as a function of the model parameters.

In the presence of wall slip, there are three flow regimes in the general case depending on the value of the wall shear stress τ_w:

(1) For $\tau_w < \tau_c$, the suspension does not flow and $Q = 0$.

(2) For $\tau_c < \tau_w < \tau_B$, the suspension slips and flows as an unyielded plug and the flow rate is given by:

11

$$Q = \beta W H [\tau_w - \tau_c] \tag{5}$$

where τ_B is the yield stress extracted from the fit of the Bingham model (ESI).

(3) For $\tau_w \geq \tau_B$, the suspension yields and the flow is due to a mix of plastic flow in the bulk and wall slip. In this case, the flow rate is given by [22]:

$$Q = \frac{W H^2 \tau_B}{6 \mu_p} \left[\frac{\tau_w}{\tau_B} - \frac{3}{2} + \frac{1}{2} \left(\frac{\tau_B}{\tau_w} \right)^2 \right] + \beta W H [\tau_w - \tau_c] \tag{6}$$

A piecewise Bingham model was used to account for shear thinning over the range of shear rates from which the rheology data was measured by updating the Bingham model parameters τ_B & μ_p to $\tau_B{}'$ & $\mu_p{}'$ respectively if $\tau_w > \tau_t$.

Knowing the flow rate Q, the flow time for one complete pass of the flow electrode, t_{pass} was obtained as the time to flow the full volume of suspension from the upper "tank" to the lower "tank":

$$t_{pass} = \frac{W H L_{travel}}{Q} \tag{7}$$

where L_{travel} is the distance traveled by the suspension.

For operation of the cell, the most important parameters are t_{pass}, which determines the charging or discharging time that is available during a single pass, and the sensitivity of the flow rate to the tilt angle, which affects how precisely the flow kinetics can be controlled. Fig. 5b shows the flow time for one pass as a function of the tilt angle θ for a GIFcell design with $H = 1.6$ mm, $W = 10$ mm and $L = 75$ mm, modeled for a zero-slip surface and for Teflon® respectively. The three flow regimes described above are outlined in the figure; note that using a Teflon® surface is beneficial in that the range of angles over which flow is neither too fast nor zero, i.e., the "elbow" of the curve, is broadened. Without wall slip, the transition from no flow to very rapid flow occurs

12

over only about 5°. Taking a tilt angle of $\theta = 10°$, for the case of Teflon® surfaces the calculated time for one pass is 3.9 min. Experimentally, a time of 3 min was observed, which is in reasonably good agreement with the model. However, the flow rate remains highly sensitive to tilt angle; for just a one degree increase in tilt angle to $\theta = 11°$, the flow time decreases from 3.9 to 2.6 min. Furthermore, a t_{pass} on the order of minutes may simply be too fast relative to the charge/discharge kinetics of the cell. (A 3 min discharge corresponds to a 20C rate for single-pass charging or discharging.) Thus, it is desirable to both slow down the flow rate and decrease the angular dependence of flow rate at the target rates.

One approach to achieve a slower flow rate of the suspension is to decrease the gap H. Fig. 5c shows the effect of decreasing H for the GIFcell for the same dimension cell with $W = 10$ mm *and L* = 75 mm, modeled for a Teflon® surface. The main result of decreasing the gap is to reduce the range of flowable angles by increasing the critical angle for onset of flow (Eqn. 2). For the range of flowable angles, the flow time for one pass is increased, but remains less than an hour for realistic values of the gap. In addition, the slope of the curve remains steep close to the onset of flow making the design difficult to control precisely in this regime.

3.4   Gas-Flow Control of Flow

A simple and precise approach for further decreasing the flow rate is to add further resistance in the form of gas flow control (Fig. 2c and 2d). Assuming incompressible (low Mach number) gas flow, mass conservation dictates that the suspension flow rate is equal to the gas flow rate (i.e. $Q_{gas} = Q$). Either an actively controlled pneumatic resistor element such as a valve, or a passive element such as a porous flow restrictor, could in principle be used. We modeled the effect

of gas flow control as follows. Neglecting the inertia of the gas (low Reynolds number), the flow resistance of the gas-flow control element is defined as:

$$\alpha = \frac{\Delta P(Q)}{Q} \tag{8}$$

where $\Delta P(Q)$ is the pressure drop across the control element for a flow rate, Q, of gas through the element. α has units of Pa.s.mm^{-3} and adds a tunable feedback loop parameter to the cell that aids in controlling the flow rate of the suspension; as the flow rate of the suspension increases, the pressure drop in the element increases and is imposed as a back pressure on the fluid and slows it down. In the case of flow through a porous medium such as a porous membrane or solid plug of a permeable medium, α is given by:

$$\alpha = \frac{L_{porous}\mu_{gas}}{\kappa A_{porous}} \tag{9}$$

where μ_{gas} is the dynamic viscosity of the gas (in our case, it is Argon), $L_{porous}, A_{porous}, \kappa$ are the thickness, cross-sectional area and permeability of the membrane or solid, respectively. With the additional back-pressure due to the resistance to gas-flow acting on the suspension, the shear stress at the wall is given by:

$$\tau_w = (\rho g \sin \theta - \alpha Q)\frac{H}{2} \tag{10}$$

The three regimes described previously are still present, and assuming wall slip is present, the angle for onset of flow remains similar to the no gas-flow control case and is now given by:

$$\theta_F = \sin^{-1}(\frac{2\tau_c}{\rho g H}) \tag{11}$$

In the slip regime ($\tau_c < \tau_w < \tau_B$), the flow rate is now given by:

14

$$Q_{gas-flow\ control} = \frac{\beta WH\left[\frac{H}{2}\rho g \sin\theta - \tau_c\right]}{\left[1 + \frac{\alpha\beta WH^2}{L} \frac{2}{2}\right]} = \frac{Q}{\left[1 + \frac{\alpha\beta WH^2}{L} \frac{2}{2}\right]} \tag{12}$$

When the material yields ($\tau_w > \tau_B$), the flow rate is given by Eqn. (6), where the shear stress at the wall is given by Eqn. (10). This defines an implicit equation for the flow rate that can be solved numerically once the design parameters are specified.

The effect of adding gas-flow control in the design on the flow time for one pass is shown in Fig. 5d for different flow resistance α in a GIFCell design with $H = 1.6$ mm, $W = 10$ mm, $L = 75$ mm, and assuming the optimal suspension is flowing over a Teflon® surface. We observe that adding the gas-flow control element does not affect the critical angle for onset of flow, but allows the flow time to be increased significantly over a wide range of flowable angles. In particular, tuning of the gas-flow control element decreases the flow rate in the slip regime as shown in Eqn. (12) and increases the angle for onset of yield ($\tau_w = \tau_B$). For example, at $\theta = 10°$, the flow time for one pass is 7.5, 26.4 and 212 min for $\alpha = 10^{-1}, 10^0$ & 10^1 $Pa.s.mm^{-3}$ respectively. These times demonstrate the benefit of incorporating a gas-flow control element in the design of the GIFcell in order to impose longer flow times and to improve flow rate control.

4.   GIFcell Prototyping and Validation

A GIFcell computer-aided design (CAD) model (excluding fasteners) is shown in Fig. 2d. The casing was 3D-printed from an ABS-like polymer proprietary to the manufacturer (Somos®WaterShedXC 11122, DSM). Gaskets and fasteners were made from ethylene propylene diene monomer (M-Class) rubber (EPDM), Teflon®, or stainless steel, each of which was separately shown to be chemically non-reactive with the flow catholyte and lithium metal anode

over the duration of the experimental tests. Gold-sputtered stainless steel plates were used as the current collectors, with a current collector area of 2 cm^2 being used for a single channel of electrode thickness $H = 1.6$ mm, $W = 10$ mm *and L* $= 75$ mm, as modeled above. As in our previous work[8], a porous carbon current collector is not used, since the suspended carbon provides both electronic conductivity and surface area for charge transfer The volume of flow electrode that occupies the space between current collectors, which we refer to as an "aliquot" [9], is 0.32 cm^3. The total electrolyte volume per channel is 3.75 aliquots (1.2 cm^3). Both single-channel and multi-channel devices were built and tested. Experiments were conducted in which flow rate was controlled by tilt angle alone, or with the assistance of gas flow. The preparation of the lithium polysulfide suspension, and the GIFcell assembly procedure, are detailed in the Experimental section.

Electrochemical testing was performed using a Bio-Logic VMP3 Cell Test System, using a potentiostatic protocol in which discharge was conducted at 2.05 V and charge at 2.6 V. From the voltage-capacity curves in Fig. 2a, this cycles the lithium polysulfide flow electrode within the soluble polysulfide regime where the reversible reaction is: $3 \, Li_2S_8 + 2 \, Li \rightarrow 4 \, Li_2S_6$. By remaining within the soluble regime, as opposed to precipitating Li_2S at lower cell voltage[8], the rheology of the suspension remains relatively constant. Initial electrochemical tests conducted at tilt angles of 90°, 60° and 30° (Fig. S5，ESI) showed clearly that the cell functions as intended, with the flow velocity, current and power all increasing monotonically with tilt angle. However, the total flow time was at most a minute, and each pass changed the state-of-charge (SOC) of the flow electrode by a factor of $<10^{-3}$, such that thousands of passes would be required to fully charge or discharge the cell. Thus lower tilt angle and gas flow control were used. Fig. 6 shows results for a GIFcell tilt angle 10° with respect to the horizontal, and with gas flow adjusted to obtain a total flow time for the 3.75 aliquots of ~30 min. This is defined to be one pass. A complete discharge (or charge)

cycle for the cell required 25 of such passes, with a total duration of 12.5 h (C-rate of C/12.5 h⁻¹). The current-time curves for all 25 passes during cycles 1 and 5 are displayed in Fig. S6. Each pass was obtained by simply tilting the cell to the opposing angle; the mechanical energy consumed in this process is negligible compared to the chemical energy of the cell. The mechanical energy for 25 flips of the materials in the cell is 0.032 J/g, which is in the order of ~10^{-4} of the electrochemical energy extracted for this system. (The scaling of mechanical energy with increasing GIFcell size is analyzed in ESI and shown to remain small.) The electrochemical energy efficiency for each cycle is calculated as:

$$Energy\ efficieny = \frac{V_D I_D t_D}{V_C I_C t_C} \tag{13}$$

where *V* is the potentiostatic voltage (2.05 V or 2.6 V) and *It* is the total charge, obtained by integrating the current over the 12.5 h duration of the test. The subscripts D and C represent discharging and charging respectively.

Fig. 6a shows the current density vs. time curves obtained during several of the passes within a full charge and discharge cycle. Notice that for each pass the current has its maximum value at the beginning, as expected under potentiostatic conditions, and then relaxes to a relatively constant current density. The absolute value of current density is in the range 0.5-1 mA/cm² over most of the SOC range, and decreases with increasing number of passes, simply because the overpotential decreases as the system is increasingly charged or discharged. This effect is also seen clearly in Fig. 6b, where the cumulative capacity vs time during each of the first five passes of a charge and discharge cycle is plotted. Since the equilibrium potential is a function of SOC, but the potentiostatic voltage is fixed, the overpotential will naturally diminish as the cell reaches full charge or discharge.

A high coulombic and energy efficiency was obtained during the initial cycles of the flow cell, as shown in Fig. 6c. The energy efficiency of the cell (vertical bars) is shown along with the total charge and discharge capacity through the first 5 cycles (the curves). The energy efficiency is high through the first three cycles, reaching 94.5% in the third cycle, but then diminishes in cycles 4 and 5 to ~75%. This decrease was traced to impedance growth in the cell resulting from the formation of a passivating layer (solid-electrolyte interphase, SEI) on the Li metal electrode. It is well-known for lithium sulfur systems that the soluble polysulfides give rise to a "shuttle" mechanism whereby diffusion of the polysulfide to the anode can result in the formation of insulating Li_2S. In these experiments, we used a conventional microporous polymer separator between the polysulfide catholyte and the lithium metal electrode, and added $LiNO_3$ to the electrolyte to help stabilize the SEI. Nonetheless, the formation of a passivation layer on the surface of the Li metal does occur, and is manifested as a sharp increase in cell impedance in cycles 4 and 5, shown in Fig. 7a, that accompanies the decrease in energy efficiency. Direct observation of the Li metal electrode after cycling, Fig. 7b, revealed the surface reaction layer. Thus the present cells suffer from the same SEI issues as conventional nonaqueous Li-S batteries, including the diffusion of dissolved polysulfides to the Li metal surface where they are reduced to insulating Li_2S. The development of sulfur-impermeable membranes (e.g. modified Nafion membrane[23,24]) or protection of the lithium surface (e.g., by a thin layer of carbon [25]) are possible approaches to resolving this well-known problem; the use of two flow electrodes as we ultimately envision for this approach (i.e., a full-flow cell rather than half-flow cell) would of course also obviate the Li metal SEI issue.

5.   Conclusions

We demonstrate a gravity-fed design for flow batteries, the GIFcell, which has a low part count and is well-suited for high energy density, non-Newtonian flow electrodes. Using a model lithium polysulfide – nanocarbons suspension that exemplifies a rheologically complex flow electrode, a high energy efficiency prototype GIFcell was designed, modeled, and experimentally demonstrated. This prototype uses flow channels of a geometry designed to prevent flow instabilities, high-slip surfaces designed to reduce the flow resistance that a yield stress fluid naturally experiences, and gas-flow control to reduce the electrode flow rate while having stable flow. In a half-cell configuration that pairs the lithium-polysulfide suspension catholyte with a solid lithium (anode), round-trip energy efficiency exceeding 90% is obtained in early cycling before the effects of cell impedance growth start to dominate. The results illustrate the integration of flow electrode electrochemical design, cell mechanical design, and development of electrochemical operation protocols for such devices.

Experimental

Handling and storage of suspension components, GIFcell assembly, rheological testing, and electrochemical testing were all conducted in an argon-filled glove box (MBRAUN, Newburyport, MA, US) with oxygen and moisture levels maintained below 5 and 1 ppm, respectively.

Preparation of Electrolyte and Catholyte

An electrolyte solution was formulated by adding a 1wt% of lithium nitrate ($LiNO_3$, Sigma-Aldrich) and 0.5 M lithium Bis(Trifluoromethanesulfonyl)imide (LiTFSI, Sigma-Aldrich) to triglyme (Sigma-Aldrich). The addition of $LiNO_3$ improves the passivation of lithium metal by forming a non-reactive surface to dissolved polysulfides on the lithium, which reduces capacity fading.

The catholyte was then prepared in the following steps. Lithium sulfide (Li_2S, Alfa) and sulfur (Sigma-Aldrich) was added to the electrolyte solution to prepare a sulfur concentration of 2.5 M in the solution. The mixture was stirred mechanically in an argon gas-filled glove box at a temperature of 60 °C for 12 h to obtain a dark brown lithium polysulfide (Li_2S_8) solution. Conductive carbon black (KB, Ketjenblack, ECP600JD, specific surface area of 800-1200 m^2g^{-1}, Azko Nobel Polymer Chemicals LLC, Chicago, Illinois, US) was used to provide an electronic conducting network to the otherwise insulating sulfur species. KB was weighed and mixed in a 20 ml glass vial. Half of the Li_2S_8 solution was added to the vial. KB was then added after which the remaining Li_2S_8 solution was added. This method of mixing was found to yield a more uniform suspension than by adding the solution directly to KB. The former exhibits a lower yield stress under the same viscometric testing conditions. The resulting suspension was then sealed in a vial

by black insulating tape and removed from the glove box. The vial was subjected to sonication in

an ultrasonic bath for 60 min to obtain a homogenous suspension of the catholyte.

Rheological Measurements of Suspensions

The viscometric behavior of the different solutions and semi-solid suspensions was

measured using a Malvern Kinexus Pro torsional rheometer enclosed in a glove box. Steady shear

viscometry tests were performed using a smooth parallel plate geometry (D = 40 mm; mean

roughness R_q = 0.36 µm). All tests were performed at 25 °C and the temperature was regulated

with a Peltier plate system. All samples were pre-sheared at 100 s^{-1} prior to measurement and left

to equilibrate until the normal force has relaxed (~15 min). Steady shear tests were performed

with decreasing applied shear rates as described by Ovarlez et al.[26] to insure the yield stress for the

material can be reached during the measurement and to avoid possible transient shear banding. In

addition, following the protocol proposed by Yoshimura & Prud'Homme [20], the same sample was

tested at three different gaps (H = 1, 0.66, 0.5 and 0.4 mm respectively) to probe and correct for

slip effects. If the flow curves at different gap distances are approximately equivalent, the material

does not slip. If gap-dependent rheology is observed, a correction needs to be applied to extract

the true shear rate applied on the sample at each value of the applied stress. A detailed analysis of

the multiple gap slip correction for the parallel plate geometry is provided in the ESI.

Exchange Current Density Measurements

In the galvanostatic polarization experiment, the polysulfide solution (2.5 M of Li_2S_6) was

vigorously stirred to ensure no mass-transport limitation, while a specified current was drawn from

the cell using a 3 mm glassy carbon working electrode (CH Instruments, Inc.) for 30 min. The

corresponding potential was determined as the average potential during the 30 min galvanostatic step. In the steady-state voltammetry experiments, an 11 μm carbon-fiber microelectrode (BASi, Inc) was used as a working electrode and the potential was swept cathodically at 20 mV/s from 3.24 V vs. Li+/Li to 1.24 V. Lithium metal electrodes were used as reference and counter electrodes.

Cycling Experiments in Non-flowing Half-cells

Swagelok® type cells with 0.5 mm deep wells were used. A Tonen separator soaked with electrolyte was used. All cell assembly was performed inside an argon-filled glovebox. The cells were tested on a Solartron potentiostat operating a 1400 Cell Test System.

Assembly of GIFcell Prototype

Prior to assembly of the GIFcell, the following procedures were carried out. The stainless steel current collector that would be in contact with the cathode material was sputtered with gold to reduce interfacial impedance. A thin Teflon® sheet with acrylic adhesive-backed film on one side (thickness = 0.005", McMaster) was applied to the surfaces of the GIFcell that would be in contact with active materials. To reduce the flow rate, Tonen separators were introduced into the tubing to function as gas-flow resistor. Two sheets of Tonen separator material were inserted into both ends of the tubing as a flow resistor.

The GIFcell parts were then assembled in the glove box. A thin foil of lithium (Sigma-Aldrich) was placed on a current collector and then wrapped with a micro-porous polymer separator (Tonen, average pore size of <100 nm). The wrapped current collector was then secured onto one plate of the GIFcell. A drop of electrolyte was introduced to wet the separator. The two

plates of the GIFcell were secured using bolts and nuts. The catholyte (Li_2S_8 suspension) was introduced into one side of the channel by injection with a syringe through the port. Finally, the tubing with the Tonen separators was attached to the ports to create the fully sealed GIFcell.

References

1. B. Dunn, H. Kamath and J.-M. Tarascon, *Science*, 2011, **334**, 928–35.

2. M. Skyllas-Kazacos, M. H. Chakrabarti, S. a. Hajimolana, F. S. Mjalli and M. Saleem, *J. Electrochem. Soc.*, 2011, **158**, R55.

3. Z. Yang, J. Zhang, M. C. W. Kintner-Meyer, X. Lu, D. Choi, J. P. Lemmon and J. Liu, *Chem. Rev.*, 2011, **111**, 3577–613.

4. R. M. Darling, K. G. Gallagher, J. a. Kowalski, S. Ha and F. R. Brushett, *Energy Environ. Sci.*, 2014, **7**, 3459–3477.

5. A. Z. Weber, M. M. Mench, J. P. Meyers, P. N. Ross, J. T. Gostick and Q. Liu, *J. Appl. Electrochem.*, 2011, **41**, 1137–1164.

6. W. Wang, Q. Luo, B. Li, X. Wei, L. Li and Z. Yang, *Adv. Funct. Mater.*, 2013, **23**, 970–986.

7. M. Duduta, B. Ho, V. C. Wood, P. Limthongkul, V. E. Brunini, W. C. Carter and Y.-M. Chiang, *Adv. Energy Mater.*, 2011, **1**, 511–516.

8. F. Y. Fan, W. H. Woodford, Z. Li, N. Baram, K. C. Smith, A. Helal, G. H. McKinley, W. C. Carter and Y.-M. Chiang, *Nano Lett.*, 2014, **14**, 2210–8.

9. K. C. Smith, Y.-M. Chiang and W. Craig Carter, *J. Electrochem. Soc.*, 2014, **161**, A486–A496.

10.   Z. Li, K. C. Smith, Y. Dong, N. Baram, F. Y. Fan, J. Xie, P. Limthongkul, W. C. Carter and Y.-M. Chiang, *Phys. Chem. Chem. Phys.*, 2013, **15**, 15833–9.

11.   P. Coussot, *J. Fluid Mech.*, 1999, 380, 363–376.

12.   Y. Couder, N. Gérard and M. Rabaud, *Phys. Rev. A*, 1986, **34**, 5175–5178.

13.   N. Maleki-Jirsaraei, A. Lindner, S. Rouhani and D. Bonn, *J. Phys. Condens. Matter*, 2005, 17, S1219–S1228.

14.   T. T. Al-Housseiny, P. A. Tsai and H. A. Stone, *Nat. Phys.*, 2012, **8**, 747–750.

15.   C. Neto, D. R. Evans, E. Bonaccurso, H.-J. Butt and V. S. J. Craig, *Reports Prog. Phys.*, 2005, **68**, 2859–2897.

16.   C. Aramphongphun and J. M. Castro, *Model. Simul. Mater. Sci. Eng.*, 2007, **15**, 157–170.

17.   J. R. Stokes and J. H. Telford, *J. Nonnewton. Fluid Mech.*, 2004, **124**, 137–146.

18.   H. A. Barnes, *J. Nonnewton. Fluid Mech.*, 1999, **81**, 133–178.

19.   D. M. Huang, C. Sendner, D. Horinek, R. R. Netz and L. Bocquet, *Phys. Rev. Lett.*, 2008, **101**, 226101.

20.   A. Yoshimura and R. K. Prud'homme, *J. Rheol.*, 1988, **32**, 53–67.

21.   L. L. Ferrás, J. M. Nóbrega and F. T. Pinho, *J. Nonnewton. Fluid Mech.*, 2012, **175-176**, 76–88.

22.   R. B. Bird and O. Hassager, *Dynamics of Polymeric Liquids, Vol.1: Fluid dynamics*, Wiley-Interscience, 1987.

23.   Y. Cao, X. Li, I. a Aksay, J. Lemmon, Z. Nie, Z. Yang and J. Liu, *Phys. Chem. Chem. Phys.*, 2011, **13**, 7660–5.

24.   J.-Q. Huang, Q. Zhang, H.-J. Peng, X.-Y. Liu, W.-Z. Qian and F. Wei, *Energy Environ. Sci.*, 2014, **7**, 347.

25.   G. Zheng, S. W. Lee, Z. Liang, H.-W. Lee, K. Yan, H. Yao, H. Wang, W. Li, S. Chu and Y. Cui, *Nat. Nanotechnol.*, 2014, **9**, 618–623.

26.   G. Ovarlez, K. Krishan, J. Goyon and P. Coussot, *J. Nonnewton. Fluid Mech.*, 2013, **193**, 68–79.

Figure Legends

Figure 1: Conventional redox flow battery design versus new scheme. (a) A conventional redox flow battery consists of two fluid tanks, from which catholyte and anolyte are mechanically pumped through the electrochemical cell stack. (b) The gravity-induced flow cell (GIFcell) has an operational principle analogous to that of an hourglass, relying on gravity to move the catholyte and anolyte through the power-extracting stack. The flow rate is controlled by tilt angle, cell design, and surface engineering for fluid slip. Electrochemical performance such as power and efficiency is controlled by the flow rate, stack design, and the inherent properties of the flow electrodes. Reversal of flow by flipping the GIFcell allows switching between charge and discharge cycles as well as multiple-pass operation during either half-cycle.

Figure 2: (a) The Li-Li$_2$S$_8$ reaction during the 1st galvanostatic cycle in a Swagelok half-cell configuration at a C-rate of 1/50 h^{-1}. The lithiation of soluble Li-PS species from Li$_2$S$_8$ to Li$_2$S$_6$ is reflected by the first 200 mAh/g of capacity, during which the voltage decreases from 2.4 to 2.05 V. Further lithiation of the Li-PS results in precipitation of insoluble Li$_2$S at a near-constant voltage of ~2.05 V. Results are for catholyte having 2.5 moles S/liter Li$_2$S$_8$ in triglyme, 0.5vol% KB, 0.5 M LiTFSI, and 1wt% LiNO$_3$. (b) First generation laboratory-scale prototype of gravity-induced flow cell (GIFcell) fabricated by 3-dimensional printing of major components. The design is a half-flow-cell with flowing catholyte and stationary Li metal counter-electrode. The internal volume ratio of storage "tanks" to electrochemical stack is ~4:1, and flow channel has high width to thickness aspect ratio. (c) Schematic of improved design combining gravity feed with passive gas flow rate controller. The notations used are the flow modeling parameters. (d) Exploded view of components for the GIFcell design in (c).

Figure 3: Selection criteria for an optimal polysulfide flow catholyte based on electrochemical and rheological considerations. (a) Voltage-capacity profile for Li metal/Li-polysulfide suspension (Li/Li-PS) electrochemical couples tested in a stationary cell configuration (Swagelok™ cell) at C/5 rate. Of the three glyme solvents for which results are shown, triglyme offers optimal tradeoff between volatility and electrochemical performance. In all cases the catholyte consists of a 2.5 M Li-PS suspension containing 1vol% ketjen black for electronic conductivity, 0.5 M LiTFSI salt, and 1 wt% LiNO$_3$ additive for anode passivation. (b) Slip-corrected flow curves measured at 25°C show similar rheology behavior for the three suspensions, indicating that carbon content dominates rheological behavior. (c) Effect of Ketjenblack (KB) loading (vol%) on the slip-corrected flow curves measured at 25 °C for 2.5 M Li-PS triglyme suspensions. The experimentally measured profiles are fitted to the Herschel-Bulkley model (solid lines) and the piecewise Bingham plastic model (dashed line). (d) Relationship between the yield stress and electronic conductivity for the

triglyme suspensions as a function of KB loading, showing that both increase with KB loading. The color contour scale shows the calculated tilt angle for onset of flow (θ_o) in a GIFcell as a function of the yield stress, at constant flow channel thickness of $H = 1.6$ mm and assuming no-slip boundary conditions.

Figure 4: Stability of flow front for a 2.5 M Li-PS suspension (0.5vol% KB, 0.5 M LiTFSI and 1wt% LiNO$_3$ in triglyme) of constant thickness $H = 1.6$ mm and different channel widths W. The suspension was injected at the top of the channel in each instance, and allowed to flow under gravity alone at 10° tilt angle above the horizontal. Top images show start of the flow test and bottom images show flow morphology at times t labeled. A uniform flow front is observed for for $W = 10$ mm, whereas viscous fingering due to Taylor-Saffman instability is observed for $W = 15$ and 30 mm. A movie of this test is available in SI (Movie S1).

Figure 5: Experimental and flow modeling results showing the effects of adjustable parameters in the GIFcell design on flow characteristics for a 2.5 M Li-PS suspension in triglyme (0.5vol% KB, 0.5 M LiTFSI and 1wt% LiNO$_3$). (a) Measured slip velocity of the suspension vs. applied shear stress at 25 °C for flow on Teflon® and stainless steel surfaces, showing the much greater slip velocity on the former. The critical slip model (Eqns. 3 and 4) was fitted as shown by the solid lines. (b) Modeling results showing flow time for a single pass vs. tilt angle. The effect of added slip from a Teflon® surface on flow time shows that increasing slip permits flow at lower angles. The desired behavior for the GIFcell is controlled, slow flow rates (long flow time) at easily controlled tilt angles. (c) Effect of flow channel thickness (H) on the flow time for one pass, showing that decreasing H slows the flow rate at fixed angle. (d) Effect of introducing gas flow control on the flow time for one pass. Gas flow resistance of the control element is defined as $\alpha = \frac{\Delta P(Q)}{Q}$ where $\Delta P(Q)$ is the pressure drop across the control element for a flow rate Q of gas through the element. α has units of Pa.s.mm^{-3}. Results show that gas flow control reduces the slope of the curves at long flow times, decreasing the sensitivity of flow rate to tilt angle and facilitating flow rate control over a wide range of tilt angles.

Figure 6: (a) The current density extracted during multiple passes of the GIFcell under potentiostatic charging at 2.60 V and potentiostatic discharging at 2.05 V. Each pass takes 30 min, while a complete charge/discharge cycle requires 25 passes. (b) Cumulative capacity vs. time during multiple discharge/charge cycles. Each half-cycle shown includes 25 passes. (c) Energy efficiency and cumulative capacity for five cycles of the GIFcell.

Figure 7: (a) Electrochemical impedance spectroscopy of the GIFcell taken at the start of 5 consecutive charg/discharge cycles, showing large impedance rise attributed to the lithium metal stationary electrode in cycles 4 and 5, corresponding to capacity and efficiency loss in Fig. 6c. (b) Micrographs of the lithium metal surface after the 5th cycle show SEI formation and precipitation of Li_2S on the lithium metal. This is due to the reduction of soluble species of lithium polysulfide during electro-cycling to Li_2S, resulting in the impedance growth with cycle number shown in (a).

Table 1: Vapor pressures of the glyme-solvent family, and the ionic conductivities and viscosities of 2.5 M lithium polysulfide (Li_2S_8) solution with the additives (0.5M LiTFSI and 1wt% $LiNO_3$) with various solvent of the glyme family.

| Solvent | Vapor Pressure (mm Hg) @ 20 °C | Ionic Conductivity (mS/cm) @ 25 °C | | Viscosity (mPa.s) |
		0.5M LiTFSI, 1wt% LiNO3[*]	0.5M LiTFSI, 1wt% LiNO3, 2.5M Li2S8[*]	0.5M LiTFSI, 1wt% LiNO3, 2.5M Li2S8
Diglyme	3	5	3.31	9
Triglyme	0.9	3.7	3.09	17
Tetraglyme	<0.01	2.14	2.00	25

Figure 1: Conventional redox flow battery design versus new scheme. (a) A conventional redox flow battery consists of two fluid tanks, from which catholyte and anolyte are mechanically pumped through the electrochemical cell stack. (b) The gravity-induced flow cell (GIFcell) has an operational principle analogous to that of an hourglass, relying on gravity to move the catholyte and anolyte through the power-extracting stack. The flow rate is controlled by tilt angle, cell design, and surface engineering for fluid slip. Electrochemical performance such as power and efficiency is controlled by the flow rate, stack design, and the inherent properties of the flow electrodes. Reversal of flow by flipping the GIFcell allows switching between charge and discharge cycles as well as multiple-pass operation during in either half-cycle.
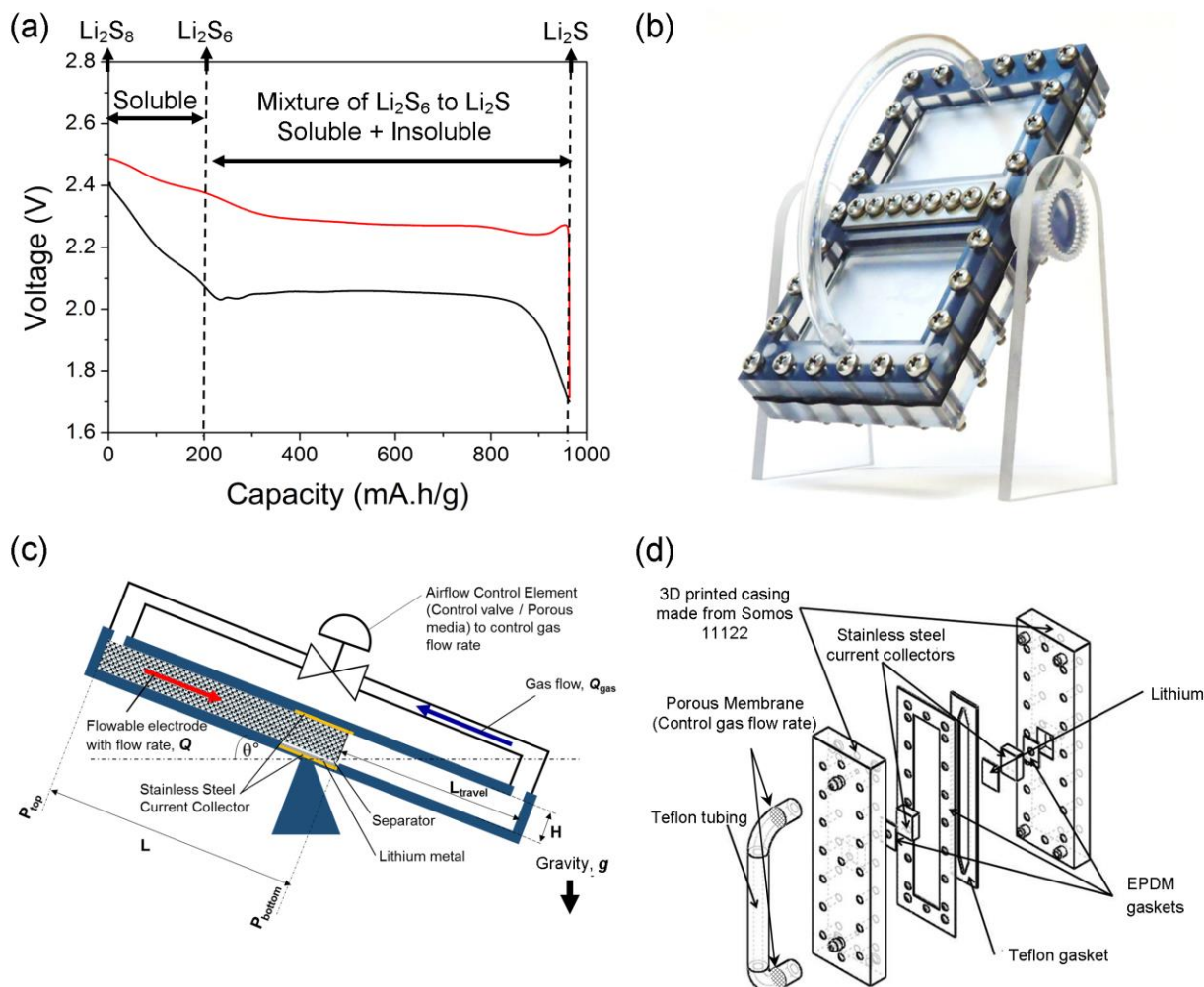
Figure 2: (a) The Li-Li$_2$S$_8$ reaction during the 1st galvanostatic cycle in a Swagelok half-cell configuration at a C-rate of 1/50 h^{-1}. The lithiation of soluble Li-PS species from Li$_2$S$_8$ to Li$_2$S$_6$ is reflected by the first 200 mAh/g of capacity, during which the voltage decreases from 2.4 to 2.05 V. Further lithiation of the Li-PS results in precipitation of insoluble Li$_2$S at a near-constant voltage of ~2.05 V. Results are for catholyte having 2.5 moles S/liter Li$_2$S$_8$ in triglyme, 0.5vol% KB, 0.5 M LiTFSI, and 1wt% LiNO$_3$. (b) First generation laboratory-scale prototype of gravity-induced flow cell (GIFcell) fabricated by 3-dimensional printing of major components. The design is a half-flow-cell with flowing catholyte and stationary Li metal counter-electrode. The internal volume ratio of storage "tanks" to electrochemical stack is ~4:1, and flow channel has high width to thickness aspect ratio. (c) Schematic of improved design combining gravity feed with passive gas flow rate controller. The notations used are the flow modeling parameters. (d) Exploded view of components for the GIFcell design in (c).
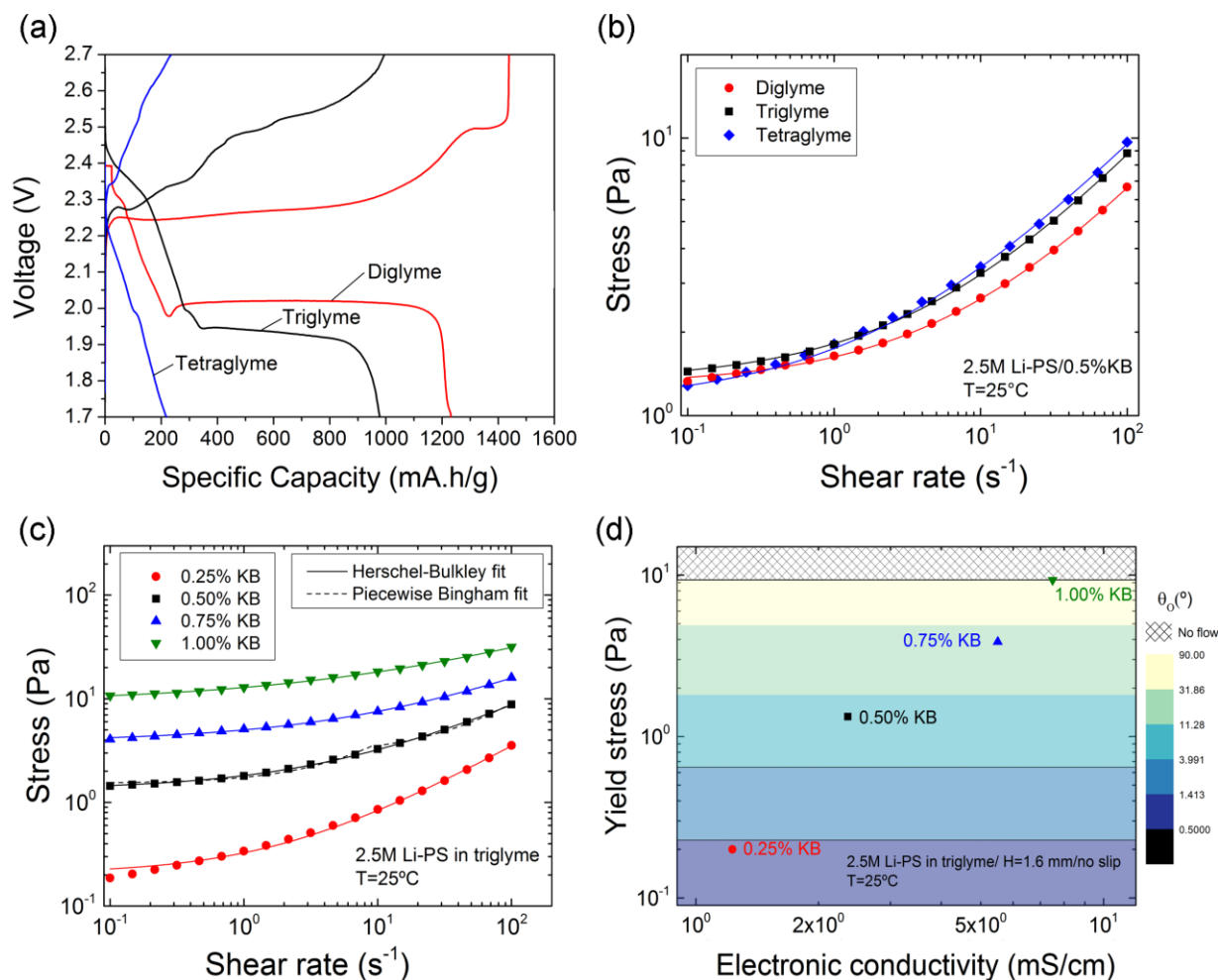
Figure 3: Selection criteria for an optimal polysulfide flow catholyte based on electrochemical and rheological considerations. (a) Voltage-capacity profile for Li metal/Li-polysulfide suspension (Li/Li-PS) electrochemical couples tested in a stationary cell configuration (Swagelok™ cell) at C/5 rate. Of the three glyme solvents for which results are shown, triglyme offers optimal tradeoff between volatility and electrochemical performance. In all cases the catholyte consists of a 2.5 M Li-PS suspension containing 1vol% ketjen black for electronic conductivity, 0.5 M LiTFSI salt, and 1 wt% $LiNO_3$ additive for anode passivation. (b) Slip-corrected flow curves measured at 25°C show similar rheology behavior for the three suspensions, indicating that carbon content dominates rheological behavior. (c) Effect of Ketjenblack (KB) loading (vol%) on the slip-corrected flow curves measured at 25 °C for 2.5 M Li-PS triglyme suspensions. The experimentally measured profiles are fitted to the Herschel-Bulkley model (solid lines) and the piecewise Bingham plastic model (dashed line). (d) Relationship between the yield stress and electronic conductivity for the triglyme suspensions as a function of KB loading, showing that both increase with KB loading. The color contour scale shows the calculated tilt angle for onset of flow (θ_o) in a GIFcell as a function of the yield stress, at constant flow channel thickness of $H = 1.6$ mm and assuming no-slip boundary conditions.
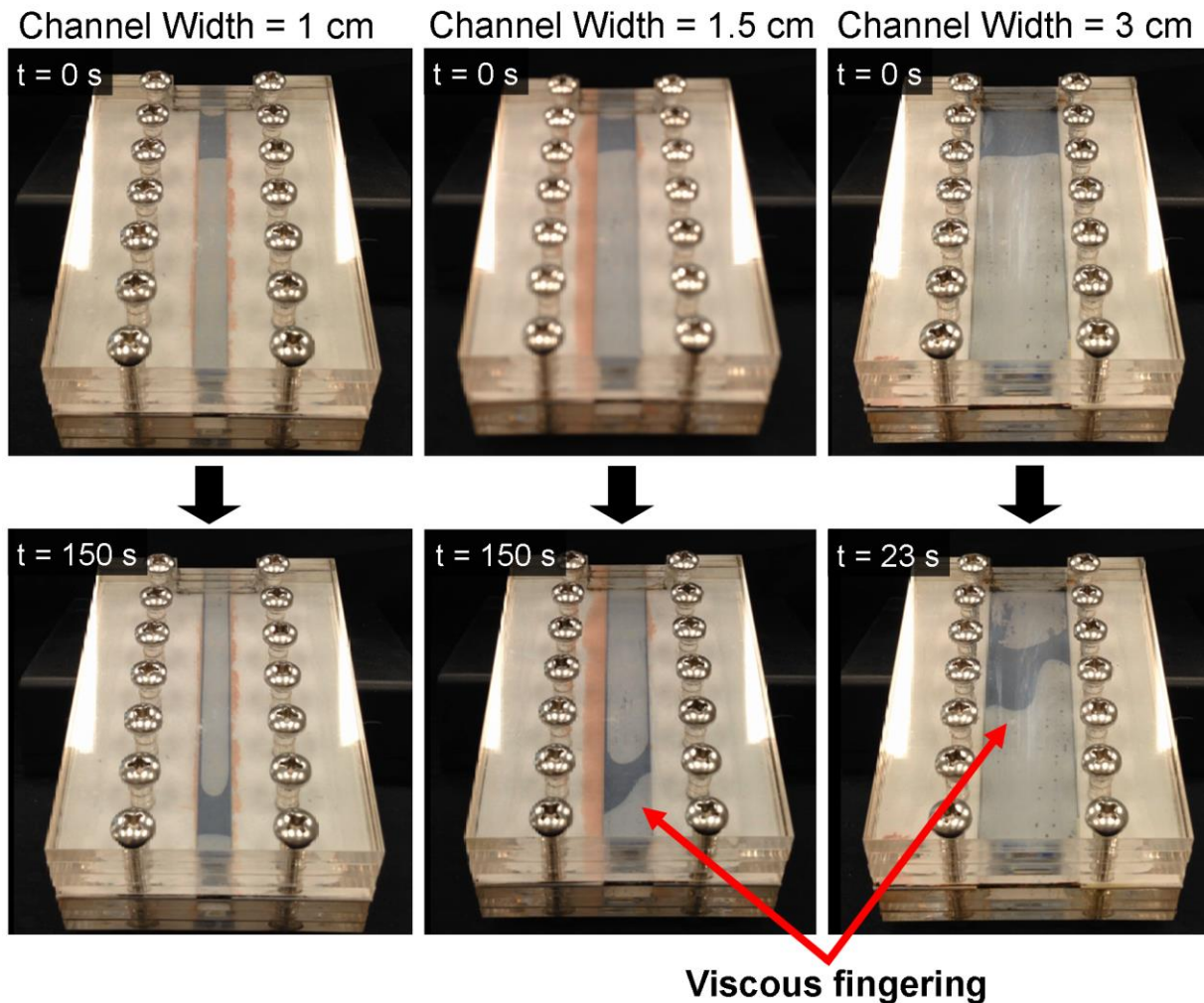
33

Figure 4: Stability of flow front for a 2.5 M Li-PS suspension (0.5vol% KB, 0.5 M LiTFSI and 1wt% $LiNO_3$ in triglyme) of constant thickness $H = 1.6$ mm and different channel widths W. The suspension was injected at the top of the channel in each instance, and allowed to flow under gravity alone at 10° tilt angle above the horizontal. Top images show start of the flow test and bottom images show flow morphology at times t labeled. A uniform flow front is observed for for $W = 10$ mm, whereas viscous fingering due to Taylor-Saffman instability is observed for $W = 15$ and 30 mm. A movie of this test is available in SI (Movie S1).
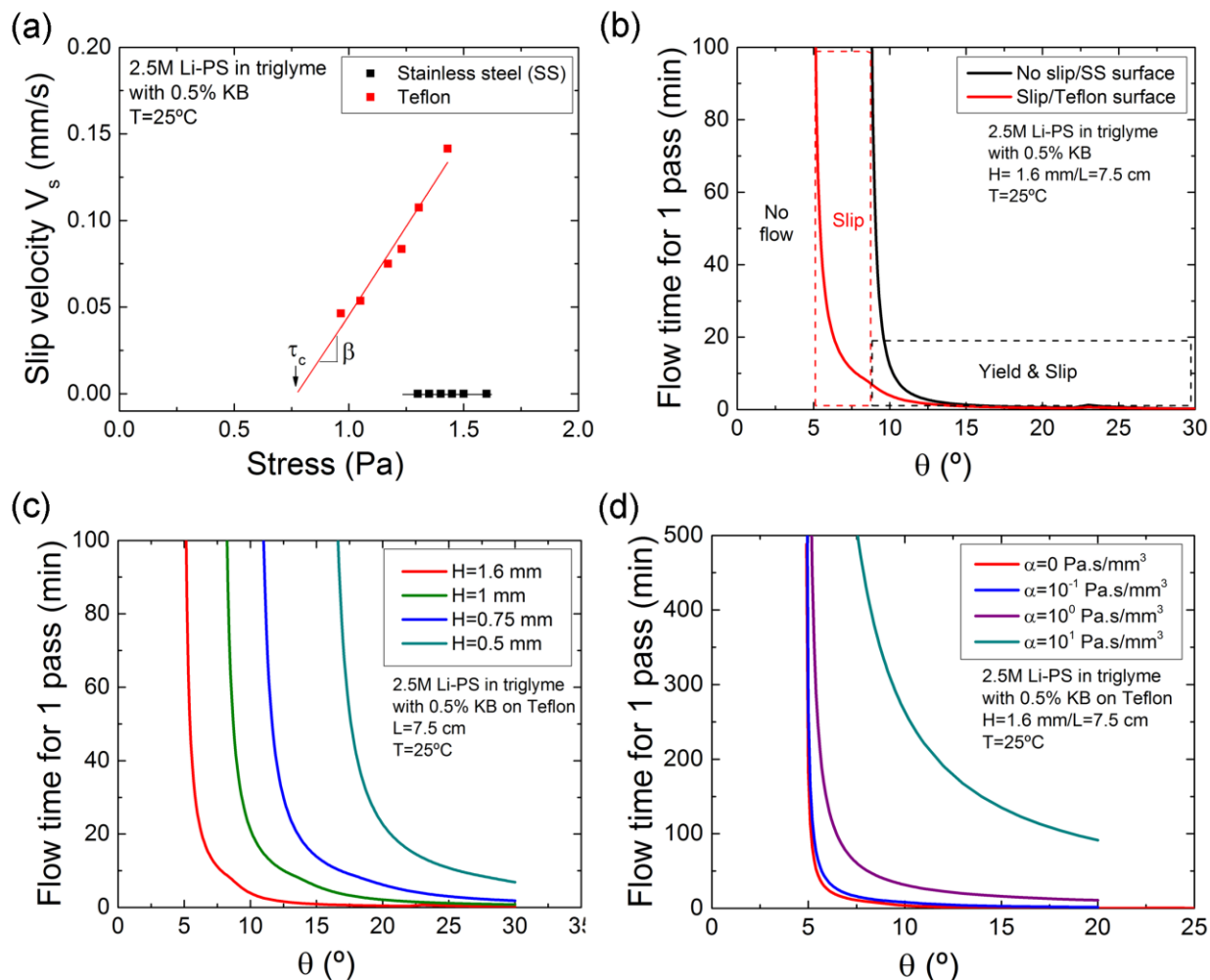
Figure 5: Experimental and flow modeling results showing the effects of adjustable parameters in the GIFcell design on flow characteristics for a 2.5 M Li-PS suspension in triglyme (0.5vol% KB, 0.5 M LiTFSI and 1wt% LiNO$_3$). (a) Measured slip velocity of the suspension vs. applied shear stress at 25 °C for flow on Teflon® and stainless steel surfaces, showing the much greater slip velocity on the former. The critical slip model (Eqns. 3 and 4) was fitted as shown by the solid lines. (b) Modeling results showing flow time for a single pass vs. tilt angle. The effect of added slip from a Teflon® surface on flow time shows that increasing slip permits flow at lower angles. The desired behavior for the GIFcell is controlled, slow flow rates (long flow time) at easily controlled tilt angles. (c) Effect of flow channel thickness (*H*) on the flow time for one pass, showing that decreasing *H* slows the flow rate at fixed angle. (d) Effect of introducing gas flow control on the flow time for one pass. Gas flow resistance of the control element is defined as $\alpha = \frac{\Delta P(Q)}{Q}$ where $\Delta P(Q)$ is the pressure drop across the control element for a flow rate Q of gas through the element. α has units of Pa.s.mm^{-3}. Results show that gas flow control reduces the slope of the curves at long flow times, decreasing the sensitivity of flow rate to tilt angle and facilitating flow rate control over a wide range of tilt angles.
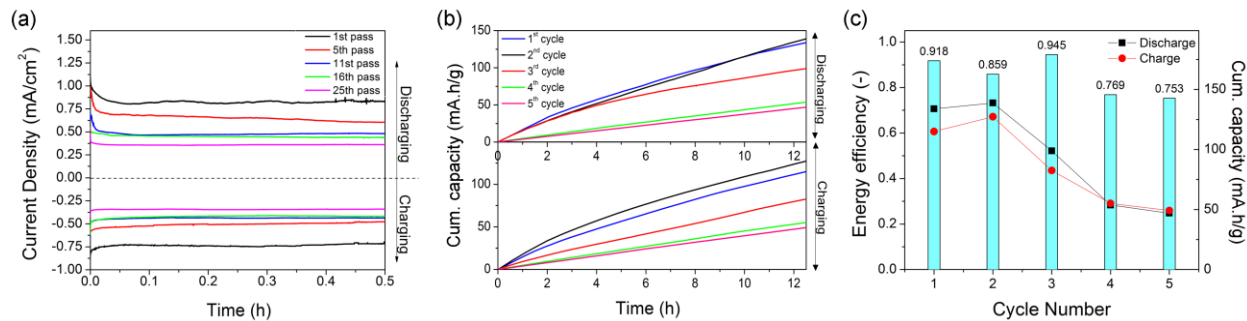
Figure 6: (a) The current density extracted during multiple passes of the GIFcell under potentiostatic charging at 2.60 V and potentiostatic discharging at 2.05 V. Each pass takes 30 min, while a complete charge/discharge cycle requires 25 passes. (b) Cumulative capacity vs. time during multiple discharge/charge cycles. Each half-cycle shown includes 25 passes. (c) Energy efficiency and cumulative capacity for five cycles of the GIFcell.
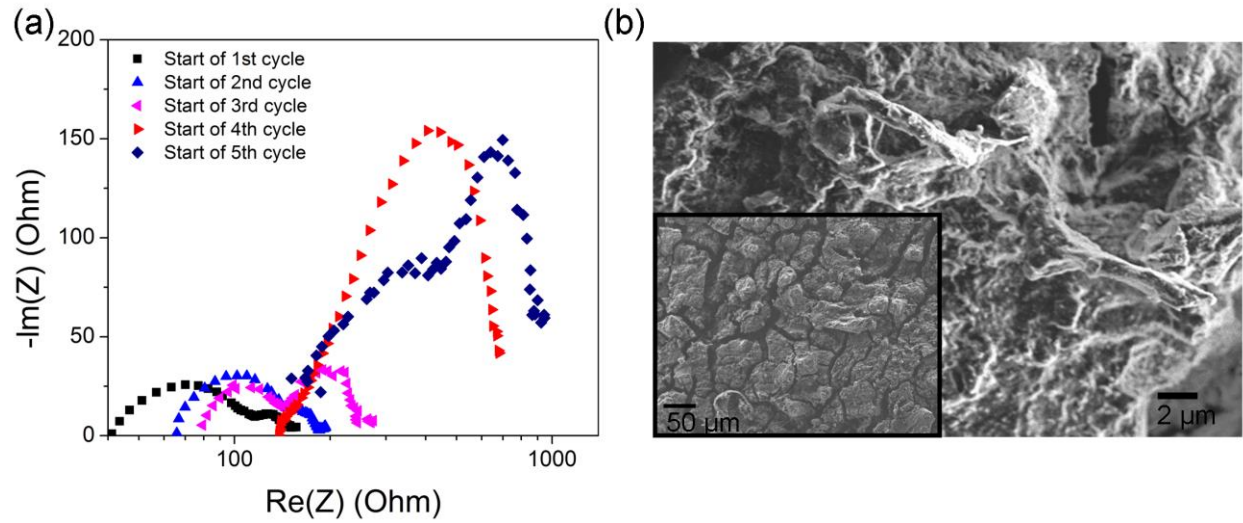
Figure 7: (a) Electrochemical impedance spectroscopy of the GIFcell taken at the start of 5 consecutive charg/discharge cycles, showing large impedance rise attributed to the lithium metal stationary electrode in cycles 4 and 5, corresponding to capacity and efficiency loss in Fig. 6c. (b) Micrographs of the lithium metal surface after the 5th cycle show SEI formation and precipitation of Li_2S on the lithium metal. This is due to the reduction of soluble species of lithium polysulfide during electro-cycling to Li_2S, resulting in the impedance growth with cycle number shown in (a).